Ocean Engineering 354 (2026) 124745

Contents lists available at ScienceDirect

Ocean Engineering

journal homepage: www.elsevier.com/locate/oceaneng

Research paper

Towards uncertainty-quantified data-driven modelling and robust control of a wave energy converter prototype

Josefredo Gadelha Da Silva [a,*], Marcio Junior Lacerda [b], Matheus Costa [a], Erivelton Nepomuceno [a,c]

[a] Department of Electronic Engineering, Centre for Ocean Energy Research, Maynooth University, W23 V5XH, Maynooth, Ireland
[b] School of Computing and Digital Media, London Metropolitan University, N7 8DB, London, UK
[c] Hamilton Institute, Maynooth University, W23 V5XH, Maynooth, Ireland

ARTICLE INFO

Keywords:
Data-driven robust control
Wave energy converter
Uncertainties
System identification
Robust control applications

ABSTRACT

This paper presents a novel unconstrained, causal, and robust H_2-norm-based control framework for wave energy converters. A data-driven model obtained from experimental measurements on a 1:20-scale Wavestar-type prototype is employed, and model uncertainty is captured through a polytopic parametrisation that defines the structure of the controlled system. Based on Lyapunov theory and Finsler's Lemma, the control synthesis conditions are formulated as linear matrix inequalities evaluated at the vertices of the polytope. The proposed controller aims to maximise energy extraction by capturing the average closed-loop energy response, providing an effective strategy for control under stochastic, broadband wave conditions. Numerical experiments demonstrate that the controller achieves efficient energy capture without violating physical constraints and outperforms the reactive, passive, and H_∞ benchmark controllers.

1. Introduction

The choice of control strategies is essential for maximising energy capture in wave energy converters (WECs), with studies reporting up to four times increase in absorbed power compared with uncontrolled devices (Ringwood et al., 2023). However, most state-of-the-art WEC controllers rely on nominal linear models derived from linear potential flow theory (LPFT) (Falnes, 2002), which neglect key nonlinear effects. Additionally, LPFT assumes small displacements, conflicting with the goal of large motions for maximum energy absorption, often leading to inconsistencies and, in extreme cases, negative power output, the so-called wave-energy paradox (Windt et al., 2021). This issue falls within the domain of model uncertainties, which are typically addressed within the framework of robust control. Robustness issues in WEC control have been discussed in Ringwood et al. (2018) and are recognised as one of the four main challenges in the field, alongside non-causality, constraint handling, and real-time implementation (Ning and Ding, 2022). This challenge arises because the governing hydrodynamic equations, namely the continuity and Navier-Stokes equations, are not inherently control-oriented. Their parameterisation into control-oriented forms, such as transfer-function or state-space models, inevitably introduces errors.

In this context, several studies have compared linear and non-linear modelling approaches for WECs. For example, Wolgamot and Fitzgerald (2015) reviewed non-linear hydrodynamic models, while Davidson and Costello (2020) analysed methods ranging from LPFT to computational fluid dynamics. Likewise, Papillon et al. (2020) highlighted the role of boundary element and integral methods in both regimes. Some works retain LPFT but compensate for non-linearities, incorporating, for instance, non-linear Froude-Krylov and restoring forces in the instantaneous wetted-surface calculation (Liu and Papanikolaou, 2011). A common finding across these studies is that non-linear models, though more accurate, are computationally demanding. Consequently, linear models are typically preferred for control synthesis due to their lower complexity and faster computation. Likewise, parameterised control-oriented models are favoured for real-time implementation and optimisation, as they enable rapid system response. However, this preference inherently reintroduces parameterisation uncertainty.

To address these issues, model-free controllers have been proposed (Anderlini et al., 2017; Zou et al., 2022). However, such methods often demand extensive training and optimisation, leading to high computational costs and limiting real-time applicability (Ning and Ding, 2022). Therefore, evaluating the reliability of different modelling and control approaches is essential, as they vary in complexity,

* Corresponding author.
E-mail addresses: josefredo.silva.2024@mumail.ie (J. Gadelha Da Silva), m.lacerda@londonmet.ac.uk (M.J. Lacerda), matheus.costa.2024@mumail.ie (M. Costa), erivelton.nepomuceno@mu.ie (E. Nepomuceno).

https://doi.org/10.1016/j.oceaneng.2026.124745
Received 18 November 2025; Received in revised form 15 January 2026; Accepted 17 February 2026

computational burden, and practical feasibility. Nevertheless, uncertainty arises not only from modelling but also from controller design. The optimal WEC control problem, aimed at maximising energy extraction, is typically formulated as an impedance-matching (IM) problem (Falnes, 2002). However, IM control is non-causal, neglects physical constraints, assumes narrowband operation inconsistent with real sea states, and requires actuators capable of power reversal due to energy injection during parts of the cycle (Fusco and Ringwood, 2013). Consequently, practical WEC controllers can only approximate the IM principle. Additionally, since IM is inherently broadband, its frequency dependence leads to an infinite-order control problem. In practice, this is addressed by narrowband design or by adopting simplified topologies such as the passive (proportional) and reactive (proportional-integral) controllers that satisfy the IM condition at a single frequency, typically the spectral peak. Other common approximations include feedforward schemes such as SaE (Fusco and Ringwood, 2013) and Lite-Con (García-Violini et al., 2020a).

To tackle this problem, Faedo and Celesti (Faedo and Celesti, 2024) discuss the implications of model-based WEC control techniques, highlighting that uncertainty in these models is typically addressed by first assuming a nominal linear WEC model, which is then extended to a family of WEC models by introducing uncertainty through synthetic data in simulation. In other words, linearly parameterised models are commonly adopted and subsequently evaluated under different realistic scenarios to assess performance and validity, even in extreme cases that violate the assumptions of the nominal model. This approach provides valuable insights into model uncertainty from the early stages of design. However, the authors advocate for the explicit consideration of modelling uncertainty and the use of experimentally derived uncertainty characterisation, rather than the synthetic variations employed in most existing studies.

In the same line, Celesti, Ferri, and Faedo (Celesti et al., 2024) highlight the value of experimental, data-driven modelling for generating families of uncertain WEC representations. Their study compares an experimentally identified model with a numerical one obtained via the boundary element solver NEMOH, based on LPFT and widely used for WEC control design. The results show distinct resonance frequencies, evidencing discrepancies between numerical and data-driven models. The authors argue that robustness challenges in WEC control persist due to non-traditional control objectives and call for explicit quantification of uncertainties within experimental models. However, uncertainty remains inherent, as data-driven models typically rely on system identification techniques.

To illustrate the robustness challenges in identified models, Farajvand et al. (2023) proposed an uncertainty estimation framework in which the so-called empirical transfer function estimate (ETFE) is modelled as an interval whose bounds depend on the input signal used during system identification. This demonstrates that, while it is often assumed that data-driven formulations can better handle uncertainty than purely model-based approaches in the context of WECs, they remain inherently uncertain, reinforcing the need for controllers explicitly designed to account for data-driven model uncertainty. A brief review of robust controllers for WECs can be found in Ringwood et al. (2023). Typically, robust control in WEC applications focuses on maximising the worst-case performance over an uncertainty set (Garcia-Violini and Ringwood, 2021; Faedo et al., 2019). Furthemore, well-known robust control techniques such as H_∞, when applied to WECs, are often formulated as non-convex problems, which can only guarantee locally optimal solutions (Lao and Scruggs, 2020).

This paper focuses on control design for the underactuated (Faedo et al., 2022) and unconstrained WEC case, where the device oscillates in a single degree of freedom, retaining only the mappings associated with the wave-excitation and control forces, and achieving energy maximisation through a state feedback-based formulation. The main contribution lies in a novel formulation of a causal robust control problem for WEC systems using the H_2 performance criteria. This represents, to the best of the authors' knowledge, the first application of the H_2 norm concept in wave-energy maximisation control, although it has previously been employed in the context of tuned mass damping, the stabilisation of floating hybrid wind-wave systems, and other offshore platforms (Martin et al., 2018; Li et al., 2025). The dataset from the open-access SWELL (Faedo et al., 2023b), produced in Aalborg University's, was employed. The data was collected using a wave basin with a 1:20-scale Wavestar-type prototype. A data-driven model with uncertainty quantification is adopted, employing a polytopic uncertainty parametrisation that renders the polytopic structure for the system to be controlled. Using the Lyapunov theory and Finsler's lemma, the control design conditions are obtained in terms of linear matrix inequalities (LMIs). Owing to the convex nature of the polytopic representation, the vertices of the polytope are used in the LMIs. Our hypothesis is that, unlike traditional robust techniques such as H_∞, which guarantee worst-case performance, the H_2 framework captures the average closed-loop energy response, offering a more natural and effective means of enhancing energy extraction from stochastic, broadband ocean waves. The numerical experiments showed that the proposed controller performs effectively in maximising energy capture without violating physical constraints, even though no explicit constraint specifications were imposed. Furthermore, it outperforms the three reference controllers used for comparison in terms of overall energy production, namely the well-established passive, and reactive controllers commonly applied in wave energy systems and a robustness-oriented H_∞ controller.

The paper is organised as follows. Section 2 presents a black-box system identification procedure used to build a continuous-time LTI state-space model for a Wavestar-type WEC prototype. This section also introduces a method for structuring uncertainty within a polytopic framework. Section 3 outlines the design procedure of the proposed H_2-norm-based controller, along with three other reference controllers. Section 4 provides a numerical evaluation of the proposed controller and compares its performance with that of the three benchmark controllers. The results are assessed under sea-state conditions derived from the SWELL dataset and from additional synthetic sea states external to it, using the identified model described in Section 2. Finally, Section 5 presents the concluding remarks.

2. Data-driven model specification

This section describes the procedure used to identify a data-driven, uncertainty-parametrised, control-oriented dynamical model for a Wavestar-type prototype. Following Faedo et al. (2023a), this study assumes that the transfer function (TF) relating the excitation and control forces to the velocity response of the WEC system can be expressed in terms of a linear operator $G : \mathbb{C} \to \mathbb{C}$ as

$$G(s) = \frac{V(s)}{F_e(s) - F_u(s)}, \tag{1}$$

where $f_e : \mathbb{R}^+ \to \mathbb{R}$ denotes the wave-excitation force due to the incident wave field, and $f_u : \mathbb{R}^+ \to \mathbb{R}$ represents the control power take-off (PTO) force. The system output corresponds to the single-mode WEC velocity $v : \mathbb{R}^+ \to \mathbb{R}$.

To identify such a linear operator, this study employs experimental data drawn from the open-access SWELL dataset (Faedo et al., 2023b), produced in Aalborg University's wave basin using a 1:20-scale Wavestar-type prototype. The dataset was specifically designed to support the validation and data-driven modelling of WEC arrays. The experimental campaign was structured into four complementary tests: Test 1 measured undisturbed free-surface elevation; Test 2 recorded wave-excitation force/torque with the device locked; Test 3 measured uncontrolled device motion; and Test 4 captured controlled motion under energy-maximising control. In this work, we adopt layout $L0$, the single-device configuration used as the baseline in the SWELL dataset. The WEC prototype is shown in Fig. 1.

The tests, layouts, and variables considered are summarised in Table 1, and the device properties are listed in Table 2.

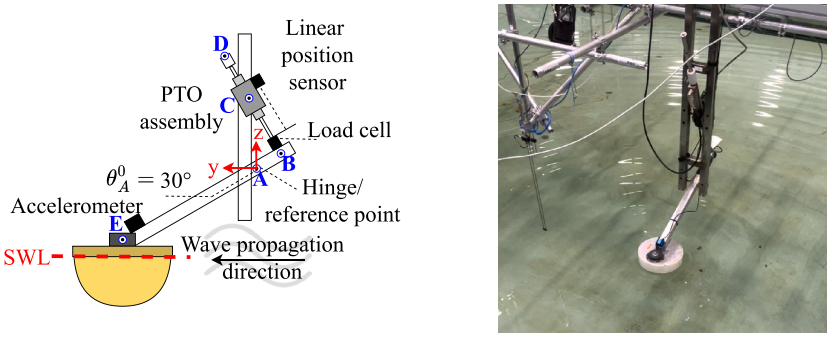

Fig. 1. Schematic and real prototype of the 1:20-scale Wavestar-type WEC (Aalborg University, May 2023).

Table 1
Dataset variables used for the torque-to-angular-velocity empirical transfer function estimation.

Layout	Sea state	Purpose	Variable (name)	Units	Test
L0	WNSS(1-3)	Excitation input	`excitationTorque_WE`	Nm	Test 2
L0	WNSS(1-3)	Velocity output	`angularVel_UM`	rad/s	Test 3
L0	shared	Time base	`time`	s	All

From Swell dataset: `Tests/L0/(17-19)_WNSS_(1-3).mat`.

Table 2
Wavestar prototype specifications.

Parameter	Value
Floater mass	4 [kg]
Inertia w.r.t. A	1 [kg m^2]
Draft	0.110 [m]
Diameter at SWL	0.256 [m]
Equilibrium angle θ_A^0	0.523 [rad]
L_{AC}	0.412 [m]
L_{CB} (equil.)	0.381 [m]
L_{AB}	0.200 [m]
L_{AE}	0.484 [m]
A-E component (y)	0.437 [m]
A-E component (z)	0.210 [m]
Centre of gravity (y)	0.415 [m]
Centre of gravity (z)	−0.206 [m]
Centre of buoyancy (y)	0.437 [m]
Centre of buoyancy (z)	−0.321 [m]
Arm mass	1.157 [kg]
Arm inertia w.r.t. A	0.060 [kg m^2]

Source: Compiled from Faedo et al. (2023b).

2.1. System identification of a control-oriented torque-angular velocity model

In this study, we apply a frequency-domain black-box identification methodology that maps the wave-excitation torque about point A (see Fig. 1) to the angular velocity response of the WEC. The excitation torque is taken from Test 2 (devices locked) and the angular velocity from Test 3 (uncontrolled motion). Let $f_e(t) := \tau_A(t)$ denote the reconstructed excitation torque (from the load-cell at B and PTO kinematics), and let $z(t) := \dot{\theta}_A(t)$ denote the angular velocity obtained via the Kalman-filter fusion described in the dataset documentation. To guarantee broadband excitation, we employ one realisation from three different white-noise sea states from SWELL (WNSS_1-WNSS_3), which exhibits an approximately flat spectral density over $[0.5, 10]$ rad/s and thus spans the dominant device dynamics.

Let $i \in \{1, 2, 3\}$ index the three white-noise levels. A *nominal* frequency response is then formed by the complex average

$$\widehat{G}_0(j\omega_k) = \frac{1}{3}\sum_{i=1}^{3}\widehat{G}_i(j\omega_k) = \frac{1}{3}\sum_{i=1}^{3}\frac{Z_i(\omega_k)}{F_{e,i}(\omega_k)}, \qquad \omega_k = \frac{2\pi k}{NT_s}, \quad N = \frac{T}{T_s}, \tag{2}$$

where $F_{e,i}(\omega_k)$ and $Z_i(\omega_k)$ are the discrete Fourier transforms of $f_{e,i}(t)$ and $z_i(t)$, respectively, for each sea state. The discrete frequency grid is given by $\omega_k = \frac{2\pi k}{NT_s}$, where T is the total record duration (300 s) and $N = T/T_s$ the number of samples. In practice, leakage and noise are mitigated by segmenting the data, applying a Hann window, and averaging over overlapping segments (Levy, 1959; Gustavsen and Semlyen, 1999; McKelvey et al., 1996; Welch, 1967). Then, Eq. (2) is used as the target for a continuous-time rational fit $G_0(s)$ obtained from

$$\min_{G\in\mathcal{R}} \sum_i \left|\widehat{G}(j\omega_k) - \widehat{G}_0(j\omega_k)\right|^2, \tag{3}$$

where $\mathcal{R}$ denotes the class of stable, strictly proper LTI models admitting a minimal state-space realisation. To quantify variability across the three sea-state levels, a magnitude envelope is formed:

$$\overline{G}(\omega_k) = \max_i \left|\widehat{G}_i(j\omega_k)\right|, \qquad \underline{G}(\omega_k) = \min_i \left|\widehat{G}_i(j\omega_k)\right|. \tag{4}$$

For each sea-state level, a fourth-order continuous-time state-space model is then fitted with stability enforced, following Ljung (1999), Pintelon and Schoukens (2012). A minimal state-space realization of the transfer function $G_i(s)$ is given by

$$G_i(s) = C_i\,(sI - A_i)^{-1}B_{e,i}, \qquad D_i = 0, \tag{5}$$

with the corresponding dynamics

$$\begin{aligned}\dot{\xi}_i(t) &= A_i\,\xi_i(t) + B_{e,i}\,\tau_{A,i}(t),\\ z_i(t) &= C_i\,\xi_i(t),\end{aligned} \tag{6}$$

where $\xi_i \in \mathbb{R}^n$ denotes the WEC state vector, $\tau_{A,i}(t) \in \mathbb{R}^{n_{\tau_A}}$ the wave-excitation torque, $z_i(t) \in \mathbb{R}^{n_z}$ the estimated output (angular velocity), and $A_i \in \mathbb{R}^{n\times n}$, $B_{e,i} \in \mathbb{R}^{n\times n_{\tau_A}}$, $C_i \in \mathbb{R}^{n_z\times n}$ are the empirical state-space matrices.

The WEC prototype under identification is known to be passive; therefore, its associated transfer function is expected to be passive (i.e., positive real). However, identified models often fail to preserve this property accurately, which may lead to undesirable effects such as numerical instabilities in simulation, non-convexities in energy-based control formulations, and unpredictable coupling between different modes of motion (Faedo et al., 2021). To ensure physical consistency, it is necessary to verify whether the corresponding ETFE obtained for each sea

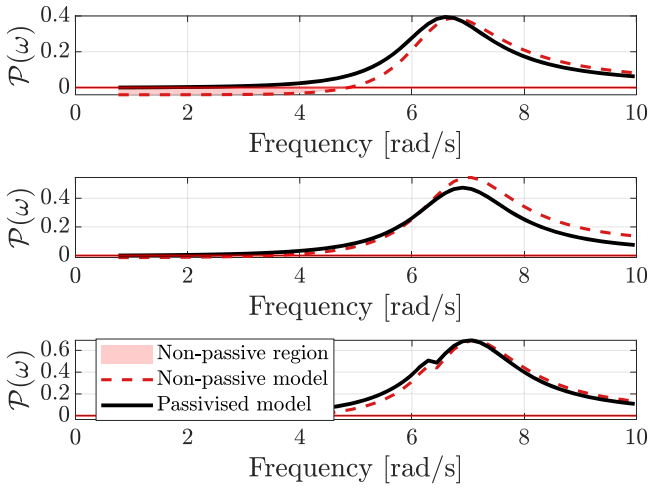

Fig. 2. Passivity indicator $\mathcal{P}_i(\omega)$ before and after LMI-based passivation for the identified *min*, *nominal*, and *max* systems. Negative values of $\mathcal{P}_i(\omega)$ indicate non-passive behaviour, whereas $\mathcal{P}_i(\omega) \geq 0$ confirms passivity.

state satisfies the passivity condition. When a violation occurs, a passivation procedure is applied by introducing an output-matrix perturbation (ΔC_i) to the system in Eq. (6), following the LMI-based approach proposed in Faedo et al. (2021), such that

$$\begin{aligned} \dot{\xi}_i(t) &= A_i\, \xi_i(t) + B_{e,i}\, \tau_{A,i}(t), \\ z_i(t) &= (C_i + \Delta C_i)\, \xi_i(t) = C_{z,i}\, \xi_i(t), \end{aligned} \tag{7}$$

while preserving the dynamics of the physical system. The passivity properties of the identified models were then evaluated using the indicator $\mathcal{P}_i(\omega)$, defined as Faedo et al. (2021)[1]

$$\mathcal{P}_i(\omega) = \lambda_{\min}\{\widehat{G}_i(j\omega) + \widehat{G}_i^{\dagger}(j\omega)\}. \tag{8}$$

If $\mathcal{P}_i(\omega) < 0$ for any $\omega \in \mathbb{R}$, the system is non-passive. Fig. 2 presents the evolution of $\mathcal{P}_i(\omega)$ before and after the LMI-based passivation for the nominal, and min-max models. As observed, the LMI-based correction ensures that all systems satisfy $\mathcal{P}_i(\omega) \geq 0$ across the entire frequency range, thus restoring the expected physical passivity of the WEC system.

Fig. 3 summarises the results of the data-driven identification procedure. It shows the passivated continuous-time state-space model identified for the nominal system, together with its passivated min-max envelope. For comparison, the hydrodynamic characterisation of the same WEC, computed via boundary-element-method (BEM) simulations using *Nemoh*,[2] is also included. The comparison between the data-driven and BEM-based models highlights differences in resonance frequency and in the amplitude and phase responses over specific frequency ranges.

Fig. 3 also presents the corresponding Nyquist diagram, which provides an intuitive visualisation of the uncertainty region associated with the identified system. Although black-box methodologies have been reported to provide highly accurate model representations and, consequently, enable more effective controller synthesis (Faedo et al., 2023a), the spread observed in the Nyquist domain demonstrates that even data-driven models inherently exhibit uncertainty. This reinforces the importance of designing robust control strategies capable of accommodating such variability.

Finally, to further assess the accuracy of the identified model, Fig. 4 compares the time-domain response of the data-driven model and the BEM-based hydrodynamic model with the experimental measurements obtained from the SWELL dataset. As observed, the data-driven model exhibits a strong agreement with the experimental response, both in amplitude and phase. This validation demonstrates that the identified continuous-time state-space representation accurately captures the dynamic characteristics of the physical system, reinforcing the reliability of the proposed data-driven identification.

The procedure described in this section follows standard practice in the wave energy literature for system identification; see, e.g., Faedo and Celesti (2024), Celesti et al. (2024), Faedo et al. (2023a). The following Section presents the uncertainty parametrisation strategy that forms the basis for the design of the robust controller.

2.2. Uncertainty parameterisation

The approach adopted in the current work rewrites the state-space representation in Eq. (7) as a controlled LTI system with *polytopic* uncertainty, thereby parametrising the variability:

$$\begin{aligned} \dot{\xi}(t) &= A(\alpha)\, \xi(t) + B_e(\alpha)\, \tau_A(t) + B(\alpha)\, f_u(t), \\ z(t) &= C_z(\alpha)\, \xi(t) + D_{zu}(\alpha)\, f_u(t), \end{aligned} \tag{9}$$

where $f_u(t) \in \mathbb{R}^{n_u}$ is the PTO control torque, and $A(\alpha) \in \mathbb{R}^{n\times n}$, $B_e(\alpha) \in \mathbb{R}^{n\times n_{\tau_A}}$, $B(\alpha) := B_e(\alpha) \in \mathbb{R}^{n\times n_u}$, $C_z(\alpha) \in \mathbb{R}^{n_z\times n}$, and $D_{zu}(\alpha) \in \mathbb{R}^{n_z\times n_u}$ are polytopic matrices.

Each polytopic matrix can be expressed as a convex combination of N vertices, such that

$$\begin{aligned} \dot{\xi}(t) &= \sum_{i=1}^{N} \alpha_i [A_i(\alpha)\, \xi(t) + B_{e,i}(\alpha)\, \tau_A(t) + B_i(\alpha)\, f_u(t)], \\ z(t) &= \sum_{i=1}^{N} \alpha_i [C_{z,i}(\alpha)\, \xi(t) + D_{zu,i}(\alpha)\, f_u(t)], \end{aligned} \tag{10}$$

where i denotes the ith vertex, and α belongs to the unit simplex

$$\Lambda_N = \left\{ \alpha \in \mathbb{R}^N \;:\; \sum_{i=1}^{N} \alpha_i = 1,\ \alpha_i \geq 0,\ i = 1, \ldots, N \right\}. \tag{11}$$

In this study, the vertices are chosen to coincide with the limits of the magnitude envelope in (4); therefore, $\alpha \in \Lambda_2$.

Remark 2.1. In the SISO case one has $n_{\tau_A} = n_u = n_z = 1$; for strictly proper models, $D_{zu}(\alpha)$ is typically zero (or numerically negligible). Additionally, a precisely known system is recovered from (9) when $N = 1$.

The uncertainty representation adopted in this work combines a data-driven origin with a parametric robust-control formulation. Specifically, the uncertainty bounds used to construct the polytopic (vertex) set are obtained from the variability observed across multiple state-space models identified directly from experimental data, under different excitation records and operating conditions. In this sense, the identification stage is inherently statistical: the resulting model dispersion reflects measurement noise, finite data length, and estimation variability, and could in principle be characterised through probabilistic tools such as parameter covariance, confidence intervals, or distributional descriptions. However, probabilistic uncertainty quantification is not the focus of this paper. Instead, we use the identified variability to define a bounded min–max envelope and treat it as a structured parametric uncertainty set for robust H_2 synthesis, yielding a single set of controller gains that is valid across the entire uncertainty range.

Consider a state-feedback control law $f_u(t) = K\, \xi(t)$ applied to the system (9), where $K \in \mathbb{R}^{n_u\times n}$ is the robust control gain that guarantees stability and performance across the entire range of uncertainty. The closed-loop system reads

$$\begin{cases} \dot{\xi}(t) = A_{cl}(\alpha)\xi(t) + B_e(\alpha)\tau_A(t), \\ z(t) = C_{z,cl}(\alpha)\xi(t) + D_{ze}(\alpha)\tau_A(t). \end{cases} \tag{12}$$

where $A_{cl}(\alpha) = A(\alpha) + B(\alpha)K$ and $C_{z,cl}(\alpha) = C_z(\alpha) + D_{zu}(\alpha)K$.

In the following, an identified dynamic model of the PTO is introduced.

[1] The operator $(\cdot)^{\dagger}$ denotes the Hermitian (conjugate) transpose, and $\lambda_{\min}$ represents the minimum eigenvalue of the system matrix.

[2] The authors acknowledge the lecturers of the course *Numerical and Experimental Modelling of Wave Energy Converters*, held at Aalborg University, Denmark, in May 2023, for providing the BEM-based model used in this work.

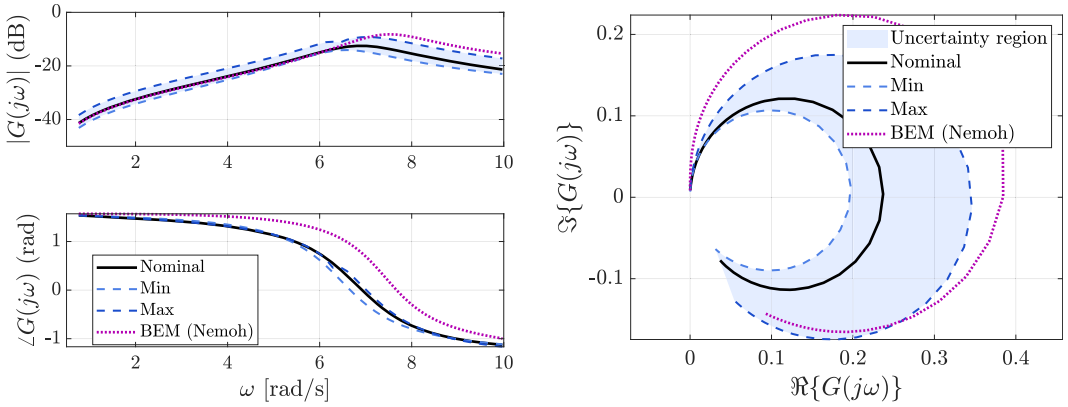

Fig. 3. Comparison between the identified data-driven and BEM-based models of the Wavestar-type WEC prototype. The left panel shows the torque-to-angular-velocity frequency response (magnitude and phase), while the right panel presents the corresponding Nyquist representation highlighting the uncertainty envelope. The black line denotes the passivated nominal continuous-time state-space fit, dashed lines indicate the min-max envelope, and the magenta dotted line corresponds to the BEM-based model obtained from *Nemoh* simulations.

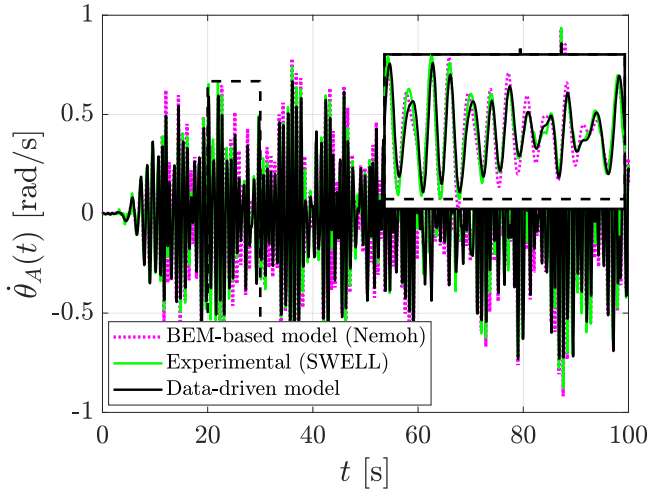

Fig. 4. Time-domain validation of the data-driven and BEM-based models against experimental measurements from the SWELL dataset. The figure compares the angular-velocity response of the Wavestar-type prototype under white-noise sea-state excitation torque (WNSS_3), showing a close correspondence between the experimental data (green), the data-driven model (black), and the BEM-based model (magenta dotted).

2.3. Characterisation of the power take-off system

In the SWELL experiments, a direct-drive linear motor (LinMot P01-37×240F) coupled with a LinMot E1200 drive was employed as the PTO system. The corresponding physical limits of the PTO are therefore defined as a maximum stroke of ±0.14 m, a peak force of ±200 N, and a maximum linear velocity of approximately 2.5 m/s.

To capture the dynamical behaviour of the actuator, the dataset provides I/O measurements consisting of a reference force signal supplied to the driver controller and the corresponding force effectively applied by the PTO system.[3] Two chirp experiments, each exciting the actuator across the frequency range relevant for WEC operation, are concatenated to construct a single identification dataset. These quantities define the mapping $f_u(t) \longrightarrow f_{u,\mathrm{PTO}}(t)$, which characterises the closed-loop behaviour of the driver–motor assembly.

Owing to the generality of the identification procedure described in the previous section, the PTO I/O data are processed in an analogous manner to obtain an empirical frequency response, from which a parametric model is subsequently fitted. A third-order transfer function is adopted to represent the dominant PTO dynamics, thereby providing an approximation of the actuator behaviour within the operating range of interest. This formulation captures the main features of the actuation chain, including bandwidth limitations and/or phase lags introduced by the embedded driver controller. Fig. 5 illustrates how the PTO dynamics are incorporated as a series element acting on the control input, so that the force delivered to the WEC is governed by

[3] From the SWELL dataset: `Linear motors/D1/IO_tests.mat`.

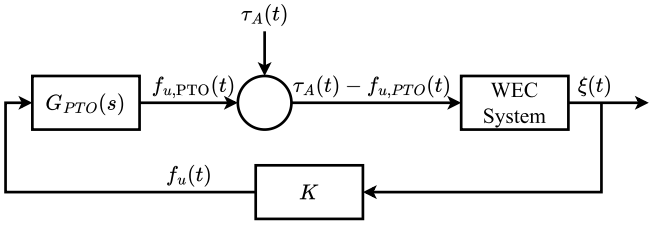

Fig. 5. Closed-loop control structure incorporating the PTO dynamics. The controller generates the reference force $f_u(t)$, which is shaped by the actuator dynamics $G_{\mathrm{PTO}}(s)$ to produce the applied PTO force $f_{u,\mathrm{PTO}}(t)$. The net torque $\tau_A(t) - f_{u,\mathrm{PTO}}(t)$ drives the WEC system, whose states $\xi(t)$ are fed back to the controller.

$$f_{u,\mathrm{PTO}}(t) = G_{\mathrm{PTO}}(s) f_u(t) = \frac{b_0}{s^3 + a_1 s^2 + a_2 s + a_3} f_u(t). \tag{13}$$

This structure preserves the separation between the hydrodynamic model and the actuator model while ensuring that all closed-loop evaluations account for the non-ideal dynamical behaviour of the PTO system.

The synthesis of the robust controller is presented in the next section.

3. Controller design

The power absorbed by the a WEC PTO is given by $P_{\mathrm{PTO}}(t) = f_{u,\mathrm{PTO}}(t)\, v_{\mathrm{PTO}}(t)$. The control objective is to maximise the correlation between these quantities, thereby increasing the extracted energy, expressed as

$$E = \int_0^T P_{\mathrm{PTO}}(t)\, dt = \int_0^T f_{u,\mathrm{PTO}}(t) v_{\mathrm{PTO}}(t)\, dt, \tag{14}$$

where T denotes the time horizon, and v_{PTO} is calculated as

$$z_{\mathrm{PTO}}(t) = \sqrt{L_{AC}^2 + L_{AB}^2 + 2 L_{AC} L_{AB} \sin(\theta_A^0 - \theta_A(t))} - L_{CB}, \tag{15}$$

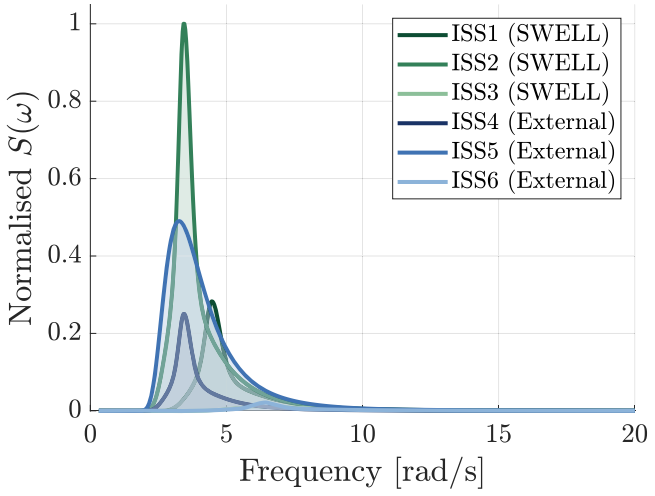

Fig. 6. Normalised spectral density functions for the irregular sea states used in controller validation. SWELL sea states are shown alongside additional synthetic cases derived from literature-based Wavestar conditions (Faedo et al., 2023a; García-Violini et al., 2020b, 2021), generated using JONSWAP spectra combined with the Nemoh first-order excitation response.

$$v_{\mathrm{PTO}}(t) = \dot{z}_{\mathrm{PTO}}(t) = -\frac{\dot{\theta}_A(t) L_{AC} L_{AB} \cos(\theta_A^0 - \theta_A(t))}{\sqrt{L_{AC}^2 + L_{AB}^2 + 2 L_{AC} L_{AB} \sin(\theta_A^0 - \theta_A(t))}}. \tag{16}$$

where $\theta_A(t)$ and $z_{\mathrm{PTO}}(t)$ denote the floater's angular displacement and the PTO arm displacement, respectively. The reader is referred to Fig. 1 and Table 2 for the definitions and dimensions of L_{AB}, L_{AC}, and θ_A^0.

Before presenting the control synthesis conditions, Finsler's Lemma and the definition of the H_2 norm are introduced.

Lemma 3.1 (Finsler's Lemma). *Let exist $\mathcal{Q} \in \mathbb{R}^{n\times n}$, and $\mathcal{Y} \in \mathbb{R}^{m\times n}$ with* $\mathrm{rank}(\mathcal{Y}) < n$. *Then, the following statements are equivalent*[4]*:*

1. $(\mathcal{Y}^{\perp})^{\top} \mathcal{Q} \mathcal{Y}^{\perp} < 0$;
2. $\exists\, \mathcal{X} \in \mathbb{R}^{n\times m}$ *such that* $\mathcal{Q} + \mathcal{X}\mathcal{Y} + \mathcal{Y}^{\top}\mathcal{X}^{\top} < 0$.

The proof can be found in deOliveira and Skelton (2001).

Definition 1. The squared H_2 norm from the impulsive input $\tau_A(t)$ to the output $z(t)$ in (9) is defined as

$$\|H_{ez}(s)\|_2^2 = \int_0^{\infty} \mathrm{Tr}\big(h(t)h(t)^{\top}\big)dt, \tag{17}$$

where $z(t) := h(t)$ is the system impulse response, and $\mathrm{Tr}(\cdot)$ denotes the trace, $A(\alpha)$ is required to be Hurwitz, and the system strictly proper (Zhou and Doyle, 1998).

The following introduces Lemmas 3.2, which characterises the H_2 performance of continuous-time polytopic LTI systems. The result applies to both uncertain and nominal (precisely known) models introduced in the previous section. A finite set of LMIs, enforced at the vertices of the polytope, is used to compute a state-feedback gain that (i) guarantees closed-loop stability when the wave-excitation torque input is zero and (ii) provides an upper bound on the H_2 performance when that input is non-zero.

Lemma 3.2. *Consider the system given by (9), given positive scalars β and ζ_2, if there exist positive definite matrices $P(\alpha) \in \mathbb{R}^{\mathbb{n}\times\mathbb{n}}$, and $X \in \mathbb{R}^{\mathbb{n}_z\times\mathbb{n}_z}$, and matrices $G \in \mathbb{R}^{\mathbb{n}\times\mathbb{n}}$, $Z \in \mathbb{R}^{\mathbb{n}_u\times\mathbb{n}}$, and $H(\alpha) \in \mathbb{R}^{\mathbb{n}_u\times\mathbb{n}_u}$, such that the following conditions hold*[5]

$$\mathrm{Tr}(X) \le \sqrt{\zeta_2}, \tag{18a}$$

$$\begin{bmatrix} -X & C_z(\alpha)G + D_{zu}(\alpha)Z \\ \star & P(\alpha) - G - G^{\top} \end{bmatrix} \le 0, \tag{18b}$$

$$\begin{bmatrix} A(\alpha)G + G^{\top}A(\alpha)^{\top} + B(\alpha)Z + Z^{\top}B(\alpha)^{\top} & P(\alpha) - G^{\top} + \beta(A(\alpha)G + B(\alpha)Z) & B_e(\alpha)H(\alpha) \\ \star & \beta(-G - G^{\top}) & 0 \\ \star & \star & \mathbf{I} - H(\alpha) - H(\alpha)^{\top} \end{bmatrix} \le 0, \tag{18c}$$

then, the state-feedback gain $K_{H2} = ZG^{-1}$, stabilises the system (9) with guaranteed cost $\|H_{ez}\|_2 \le \sqrt{\zeta_2}$, for all $\alpha \in \Lambda_N$.

Proof. Consider the solution of (12), given by $\xi(t) = e^{A_{cl}(\alpha)t}\xi(0) + \int_0^{\infty} e^{A_{cl}(\alpha)(t-\tau)} B_e(\alpha)\tau_A(\tau)d\tau$. The impulse response of the system is defined as the state trajectory when $x(0) = 0$ and the input is chosen as $\tau_A(t) = \delta(t)$, the Dirac delta function. Under these conditions, the resulting response is $h(t) = C_{z,cl}(\alpha)e^{A_{cl}(\alpha)t}B_e(\alpha)$. Therefore, (17) can be rewritten as

$$\begin{aligned} \|H_{ez}(s)\|_2^2 &= \int_0^{\infty} \mathrm{Tr}\Big(C_{z,cl}(\alpha)e^{A_{cl}(\alpha)t}B_e(\alpha)B_e(\alpha)^{\top}e^{A_{cl}(\alpha)^{\top}t}C_{z,cl}(\alpha)^{\top}\Big)dt \\ &= \mathrm{Tr}\left(C_{z,cl}(\alpha)\left(\int_0^{\infty} e^{A_{cl}(\alpha)t}B_e(\alpha)B_e(\alpha)^{\top}e^{A_{cl}(\alpha)^{\top}t}dt\right)C_{z,cl}(\alpha)^{\top}\right) \\ &= \mathrm{Tr}(C_{z,cl}(\alpha)W_c(\alpha)C_{z,cl}(\alpha)^{\top}), \end{aligned} \tag{19}$$

where $W_c(\alpha)$ denotes the controlability Gramian.

The following condition holds:

$$A_{cl}(\alpha)W_c(\alpha) + W_c(\alpha)A_{cl}(\alpha)^{\top} = -B_e(\alpha)B_e(\alpha)^{\top}. \tag{20}$$

Similarly, let there exist $P(\alpha) = P(\alpha)^{\top} \ge 0$, with $P(\alpha) \ge W_c(\alpha)$, that satisfies the Lyapunov inequality

$$\begin{aligned} &A_{cl}(\alpha)P(\alpha) + P(\alpha)A_{cl}(\alpha)^{\top} + B_e(\alpha)B_e(\alpha)^{\top} \le 0 \\ &\Rightarrow \begin{bmatrix}\mathbf{I} & A_{cl}(\alpha) & B_e(\alpha)\end{bmatrix}\begin{bmatrix} 0 & P(\alpha) & 0 \\ P(\alpha) & 0 & 0 \\ 0 & 0 & \mathbf{I}\end{bmatrix}\begin{bmatrix}\mathbf{I} \\ A_{cl}(\alpha)^{\top} \\ B_e(\alpha)^{\top}\end{bmatrix} \le 0, \end{aligned} \tag{21}$$

then, (19) can be cast in inequality form as

$$\|H_{ez}(s)\|_2^2 \le \mathrm{Tr}(C_{z,cl}(\alpha)P(\alpha)C_{z,cl}(\alpha)^{\top}). \tag{22}$$

An equivalent condition to (22) is given by

$$\begin{aligned} &\|H_{ez}\|_2^2 \le \mathrm{Tr}(X), \quad \text{s.t.} \quad C_{z,cl}(\alpha)P(\alpha)C_{z,cl}(\alpha)^{\top} - X \le 0 \\ &\Rightarrow \begin{bmatrix}\mathbf{I} & C_{z,cl}(\alpha)\end{bmatrix}\begin{bmatrix}-X & 0 \\ 0 & P(\alpha)\end{bmatrix}\begin{bmatrix}\mathbf{I} \\ C_{z,cl}(\alpha)^{\top}\end{bmatrix} \le 0, \end{aligned} \tag{23}$$

where $X \in \mathbb{R}^{n_z\times n_z}$.

The application of Finsler's lemma to (21) and (23) yields, respectively,

$$\begin{aligned} &\begin{bmatrix} 0 & P(\alpha) & 0 \\ P(\alpha) & 0 & 0 \\ 0 & 0 & \mathbf{I}\end{bmatrix} + \begin{bmatrix} X_1 & X_4 \\ X_2 & X_5 \\ X_3 & X_6\end{bmatrix}\begin{bmatrix} A_{cl}(\alpha)^{\top} & B_e(\alpha)^{\top} \\ -\mathbf{I} & 0 \\ 0 & -\mathbf{I}\end{bmatrix}^{\top} \\ &\qquad + \begin{bmatrix} A_{cl}(\alpha) & B_e(\alpha) \\ -\mathbf{I} & 0 \\ 0 & -\mathbf{I}\end{bmatrix}\begin{bmatrix} X_1^{\top} & X_4^{\top} \\ X_2^{\top} & X_5^{\top} \\ X_3^{\top} & X_6^{\top}\end{bmatrix}^{\top} \le 0, \end{aligned} \tag{24}$$

and

$$\begin{aligned} &\begin{bmatrix} -X & 0 \\ 0 & P(\alpha)\end{bmatrix} + \begin{bmatrix} -V \\ -J\end{bmatrix}\begin{bmatrix} -C_{z,cl}(\alpha)^{\top} & \mathbf{I}\end{bmatrix} + \begin{bmatrix} -C_{z,cl}(\alpha) \\ \mathbf{I}\end{bmatrix}\begin{bmatrix} -V^{\top} \\ -J^{\top}\end{bmatrix}^{\top} \le 0 \\ &\Rightarrow \quad \begin{bmatrix} -X + VC_{z,cl}(\alpha)^{\top} + C_{z,cl}(\alpha)V^{\top} & -V + C_{z,cl}(\alpha)J^{\top} \\ -V^{\top} + JC_{z,cl}(\alpha)^{\top} & P(\alpha) - J - J^{\top}\end{bmatrix} \le 0. \end{aligned} \tag{25}$$

where $X_1, \ldots, X_6$, V, and J are slack variables introduced through the application of Finsler's Lemma.

[4] $\mathcal{Y}^{\perp}$ denote a basis for the null space of $\mathcal{Y}$ (i.e., $\mathcal{Y}\mathcal{Y}^{\perp} = 0$).

[5] $\mathbf{I} \in \mathbb{R}^{n_u}$ is the identity matrix, and $\star$ denotes the symmetric completion of the block.

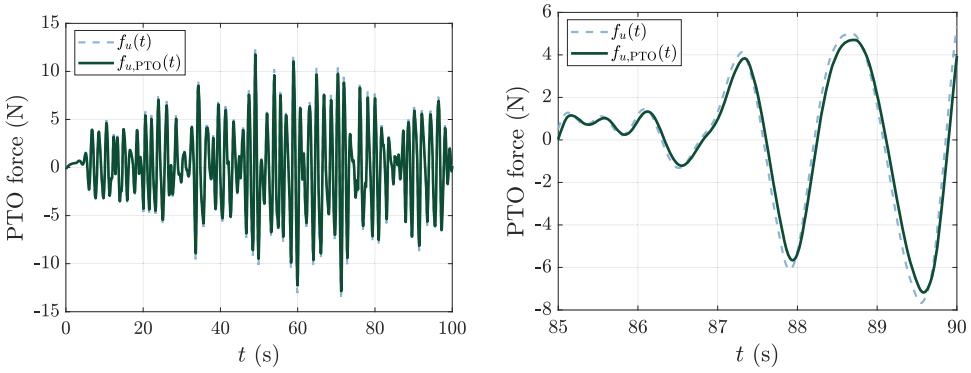

Fig. 7. Reference control force $f_u(t)$ and applied PTO force $f_{u,\mathrm{PTO}}(t)$ for the H_2 controller under the most energetic sea state (ISS2). The zoomed view highlights the phase lag and amplitude attenuation introduced by the PTO dynamics.

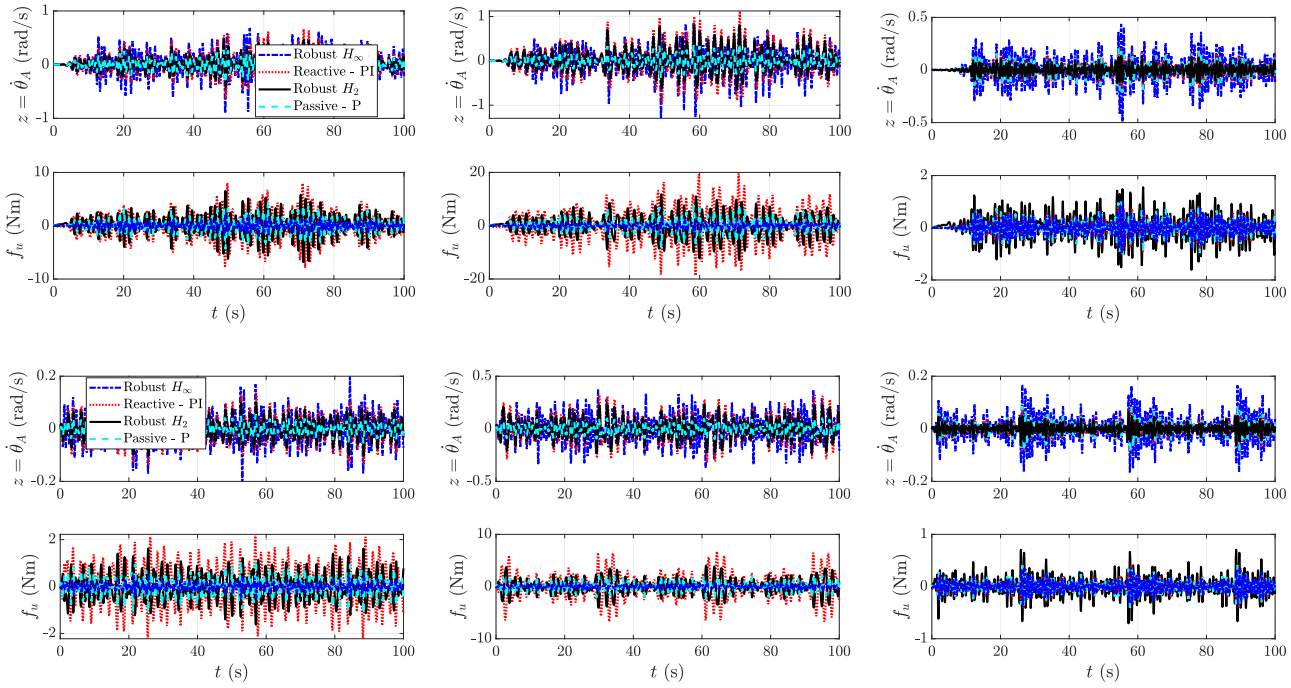

Fig. 8. Comparison of the proposed robust H_2 controller with the passive, reactive and H_∞ strategies for different sea states. The top plots show a time snippet of the WEC angular velocity, while the bottom plots present the corresponding control torque, with the subplots corresponding to ISS1–ISS6 from left to right and from top to bottom, respectively.

By choosing $V = 0$, $J = G^\top$, $X_1 = G^\top$, $X_2 = \beta G^\top$, $X_6 = H(\alpha)^\top$, $X_3 = X_4 = X_5 = 0$, and $Z = KG$, a convex realisation is obtained, and the LMIs in (18b) and (18c) are recovered, which concludes the proof. Furthermore, the conservatism of the LMIs can be reduced by employing parameter-dependent matrices defined as homogeneous polynomially parameter-dependent variables of arbitrary degree. This motivates the dependence of $P(\alpha)$ and $H(\alpha)$ on the scheduling parameter. □ □

In this study, LMIs (18a)–(18c) ensure an upper bound $\sqrt{\zeta_2}$ on the norm H_2 from the impulsive input $\tau_A(t)$ to the output $z(t)$. The energy-maximisation goal is achieved by relaxing ζ_2, thus amplifying the variance of the angular-velocity response to random wave-excitation torque.

3.1. Reference controllers

Before proceeding with the performance analysis of the controller proposed in this work, three well-known benchmark controllers are introduced for comparison. The first is the so-called passive (proportional) controller, which represents one of the most classical IM-based strategies in the literature and is typically adopted as a reference case for WEC controllers (see, e.g., Faedo et al., 2023a,b; Sun et al., 2023). The second is a reactive (proportional-integral) controller, which extends the IM-based formulation by introducing a phase-compensating term to approximate the complex-valued optimal control impedance. The third is the well-established H_∞ controller, which serves as a representative robust control strategy, enabling a meaningful comparison with other robustness-oriented approaches. The design conditions for all controllers are outlined below:

Passive controller:

This controller belongs to the class of IM-based WEC control strategies, in which the optimality conditions are approximated through a feedback architecture such that the control force in Eq. (9) is defined as

$$f_u = K_p\, z(t), \tag{26}$$

where K_p denotes a proportional control gain obtained by interpolating the unconstrained optimal frequency-domain energy maximisation condition associated with $G_0(s)$ (see Eq. (3)) (Faedo et al., 2023a).

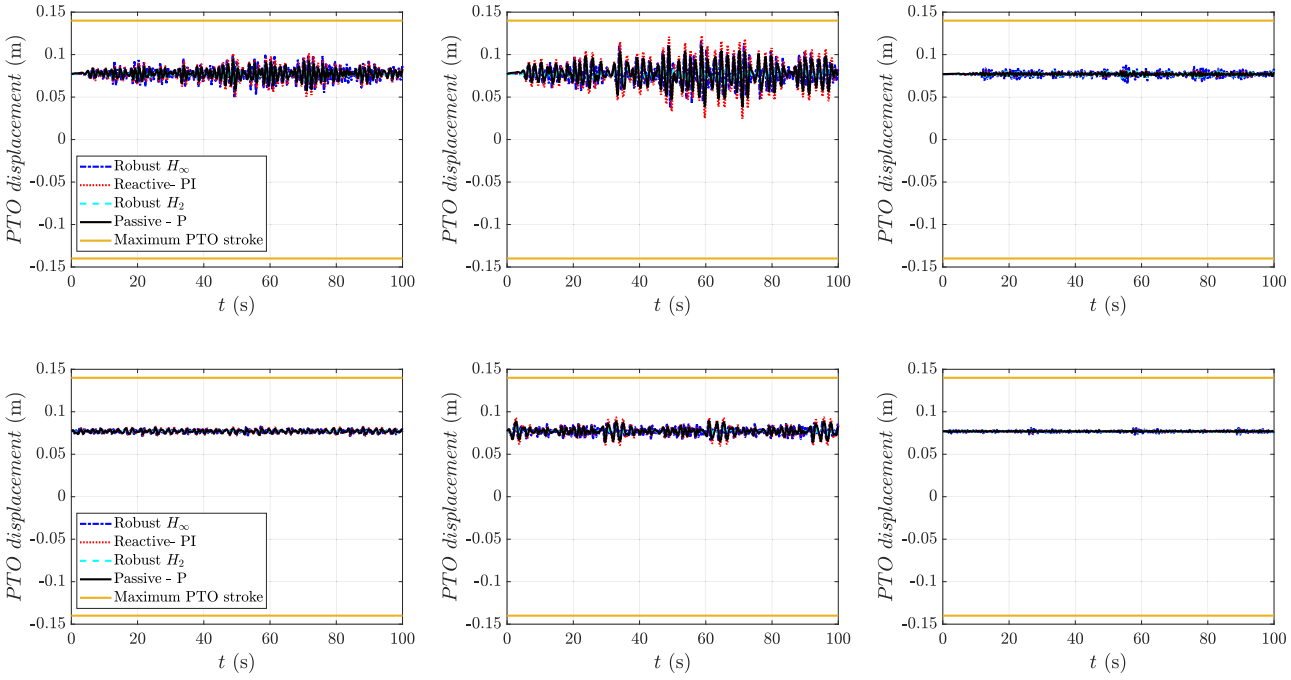

Fig. 9. Time snippet of the WEC PTO displacement. For all controllers, the PTO remains within acceptable limits for the considered sea states. The subplots correspond to ISS1–ISS6 from left to right and from top to bottom, respectively.

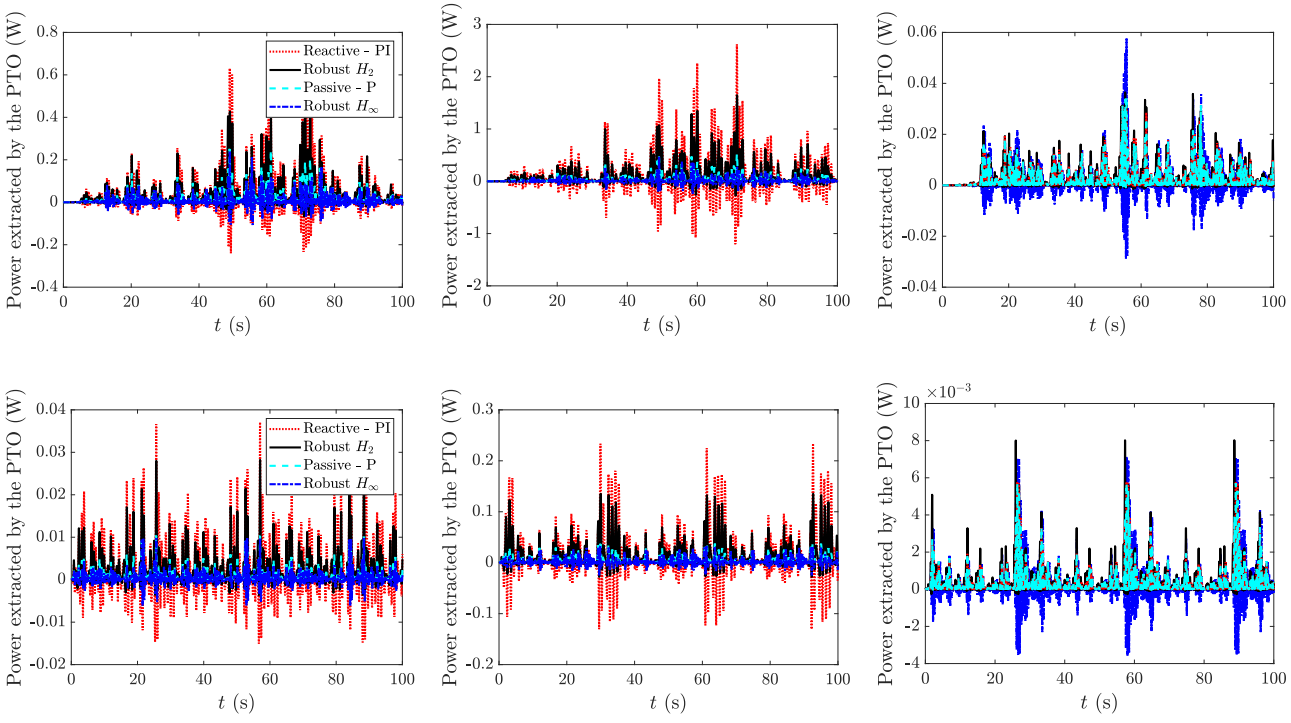

Fig. 10. Time snippet of the instantaneous PTO power for different control strategies and sea states. Results are shown for ISS1–ISS6 from left to right and from top to bottom, respectively. The reactive, H_2, and H_∞ strategies inject power back into the system during part of the cycle.

Reactive controller:

This controller also belongs to the family of IM-based WEC control strategies, but differs from the passive case in that it explicitly introduces a phase-compensating term to approximate the complex-valued optimal control law. In this case, the control force in Eq. (9) is defined as

$$f_u = K_r\, z(t) + K_i \int z(t)dt, \tag{27}$$

where K_r and K_i denote, respectively, the reactive (velocity-dependent) and in-phase (displacement-dependent) gains. These coefficients are obtained by interpolating the unconstrained frequency-domain optimality conditions associated with $G_0(s)$ and enforcing the approximate real and imaginary components of the optimal control impedance. This structure enables the controller to emulate the ideal reactive power flow required for maximising energy extraction while providing a causal, im-

plementable approximation suitable for comparison with the proposed robust control framework.

Further details on the application of the IM principle for the computation of the K_p, K_r, and K_i gains can be found in Faedo et al. (2022). For the IM-based benchmark controllers (passive and reactive), the gains are tuned separately for each sea state, since the IM interpolation is performed at a characteristic frequency, taken here as the sea-state peak frequency. For each evaluation case, the peak frequency is computed from the peak period T_p reported in Table 3.

H_∞ controller:

The reader is referred to da Silva et al. (2025), Agulhari et al. (2010) for definition of $\|H_{ez}\|_\infty$ norm and further details on the design conditions of this controller. The following Lemma is employed to design the H_∞ controller.

Lemma 3.3. *Consider the system given by Eq. (9), given positive scalars β and ζ_∞, if there exist positive definite matrix $P \in \mathbb{R}^{\mathbb{n}\times\mathbb{n}}$, and matrices $G \in \mathbb{R}^{\mathbb{n}\times\mathbb{n}}$, $Z \in \mathbb{R}^{\mathbb{m}_u\times\mathbb{n}}$, and $H \in \mathbb{R}^{\mathbb{m}_u\times\mathbb{m}_u}$ such that*

$$\mu \leq \sqrt{\zeta_\infty}, \tag{28a}$$

$$\begin{bmatrix} A(\alpha)G + G^\top A(\alpha)^\top + B(\alpha)Z + Z^\top B(\alpha)^\top & \star & \star & \star \\ P - G^\top + \beta(A(\alpha)G + B(\alpha)Z)^\top & \beta(G + G^\top) & \star & \star \\ C_z(\alpha)G + D_{zu}(\alpha)Z & \beta\big(C_z(\alpha)G + D_{zu}(\alpha)Z\big) & -\mu\mathbf{I} & \star \\ -H^\top B_e(\alpha)^\top & 0 & 0 & \mathbf{I} + H + H^\top \end{bmatrix} < 0, \tag{28b}$$

then, the the state feedback gain $K_{H\infty} = ZG^{-1}$ stabilises the system with a guaranteed cost $\|H_{ez}\|_\infty \leq \sqrt{\mu}, \mu \in \mathbb{R}, \forall\alpha \in \Lambda_N$.

Once again, the energy maximisation objective is attained through the relaxation of the design parameter ζ_∞.

4. Numerical results

This section presents a numerical assessment of the simulation results obtained by applying the robust H_2 controller described in the previous section to the system characterised in Section 2. The controller gain was computed by formulating and solving the LMI conditions using semi-definite programming algorithms implemented via the YALMIP parser (Löfberg, 2004), the ROLMIP toolbox (Agulhari et al., 2019), and the SeDuMi solver (Sturm, 1999). Unless stated otherwise, all the cases presented in this section refer to the nominal model, $G_0(s)$, introduced in Section 2. Furthermore, the present study focuses exclusively on the unconstrained case, in which no explicit physical or operational constraints are imposed during the control design. The analysis is therefore limited to verifying whether the control effort and the resulting floater motion remain within the PTO limits indicated in Section 2.3.

4.1. Sea-state specifications

For validation purposes, additional sea-state conditions from the SWELL dataset were considered, as reported in Table 3, namely three distinct irregular sea states (ISSs) characterised by the JONSWAP spectrum (Ning and Ding, 2022)

$$S(\omega) = \Gamma g^2 \omega^{-5} \exp\left[-\frac{5}{4}\left(\frac{\omega_p}{\omega}\right)^4\right] \gamma^{\exp\left[-\frac{(\omega-\omega_p)^2}{2\sigma^2\omega_p^2}\right]}, \tag{29}$$

where $S(\omega)$ denotes the spectral density function (SDF), ω is the angular frequency, ω_p is the peak frequency, Γ is the Phillips scaling parameter, γ is the JONSWAP peak enhancement factor, σ is the spectral width parameter, and g is the gravitational acceleration. These ISSs were selected not only because they correspond to the same conditions implemented in SWELL, namely: two narrow-banded cases with different wave heights and one broadband case with low, WEC-resonant, and high-frequency components; but also to evaluate how the proposed controller responds to inputs different from those used for system identification. In practice, this represents a realistic scenario, since ocean waves are inherently random and can be described by stochastic descriptors such as those defining the implemented ISSs. Furthermore, the SWELL authors have also made publicly available the IM-based control case for these ISSs, which serve as useful benchmarks for comparison.

In addition to the SWELL conditions, three further irregular sea states (ISS4-ISS6) not originating from the SWELL campaign were also considered for validation. These external sea states were selected from representative conditions reported in the literature for the Wavestar WEC prototype (Faedo et al., 2023a; García-Violini et al., 2020b, 2021). For these cases, the external conditions were generated by combining a JONSWAP spectral description with the first-order pitch excitation response obtained from the Nemoh hydrodynamic model of the device. A realisation of the free-surface elevation $\eta(t)$ was then generated by discretising (29) and applying a random-phase reconstruction:

$$\eta(t) = \sum_{k=1}^{N_f} \sqrt{2\,S(\omega_k)\,\Delta\omega}\,\cos\big(\omega_k t + \phi_k\big), \tag{30}$$

where N_f is the number of frequency components, ω_k is the kth angular frequency sample, $\Delta\omega$ is the frequency discretisation step, and ϕ_k are independent random phases uniformly distributed in $[0, 2\pi)$.The excitation impulse response function was obtained from the inverse Fourier transform of the first-order pitch excitation moment RAO $F_{\text{exc}}(\omega)$ computed using Nemoh:

$$h_{\text{exc}}(t) = \mathcal{F}^{-1}\big\{F_{\text{exc}}(\omega)\big\}, \tag{31}$$

where $F_{\text{exc}}(\omega)$ represents the frequency-domain excitation moment and $h_{\text{exc}}(t)$ is the corresponding excitation impulse response function. Finally, the excitation torque $\tau_A(t)$ was obtained by convolving the generated elevation signal with the excitation impulse response function:

$$\tau_A(t) = (h_{\text{exc}} * \eta)(t) = \int_0^\infty h_{\text{exc}}(\tau)\,\eta(t-\tau)\,d\tau. \tag{32}$$

This procedure yields physically consistent hydrodynamic forcing while remaining fully independent from the SWELL dataset, thereby enabling a broader and more robust validation of the proposed control framework. Table 3 summarises all ISSs considered for controller validation, and Fig. 6 shows the normalised SDF for each case.

4.2. Power take-off dynamics

This section examines the effect of incorporating the identified PTO dynamics on the effective control force applied to the WEC. The analysis focuses on the most energetic sea state (ISS2), for which the influence of actuator dynamics is expected to be most pronounced due to the higher control effort demanded by the controller. The actuator model is consistently included in the simulations of all control strategies considered in this study. For clarity, Fig. 7 reports results for the H_2 controller only, as a representative case; however, a similar qualitative behaviour is observed for the passive, reactive, and H_∞ controllers.

The results reveal that the corresponding PTO-applied forces are slightly smoothed and phase-shifted when compared with the reference control forces. This behaviour is consistent across all control strategies. For all controllers, the inclusion of PTO dynamics primarily manifests as a mild reduction in peak force amplitudes and a phase lag relative to the controller output. These observations highlight the importance of accounting for PTO dynamics in closed-loop simulations, as neglecting actuator behaviour may lead to overly optimistic assessments of control performance and energy extraction. Nevertheless, the results confirm that all controllers remain capable of operating within the physical limits of the PTO system, even when realistic actuator dynamics are included.

Table 3
Irregular sea-state conditions used for controller validation.

Source	Layout	Sea state	Test file / Ref.	Height H_s [m]	Period T_p [s]	Peakedness γ	Length [s]
SWELL	L0	ISS1	`11_ISS1_1`	0.063	1.412	3.3	300
SWELL	L0	ISS2	`13_ISS2_1`	0.104	1.836	3.3	300
SWELL	L0	ISS3	`15_ISS3_1`	0.0208	0.988	1.0	300
External	–	ISS4	Faedo et al. (2023a)	0.052	1.836	3.3	300
External	–	ISS5	García-Violini et al. (2021)	0.1042	1.936	1	300
External	–	ISS6	García-Violini et al. (2020b, 2021)	0.0208	0.988	3.3	300

SWELL dataset: `Tests/L0/(11-15)_ISS(1-3)_1.mat`.

Table 4
Controller tuning parameters for each ISS case.

	H_2 Controller			Passive Controller	Reactive Controller	H_∞ Controller		
ISSs	β	ζ_2	K_{H2} (solution)	K_p (solution)	$[K_r\ K_i]$ (solution)	β	ζ_∞	$K_{H\infty}$ (solution)
ISS1	1.0×10^{-1}	1.0×10^{0}	[5.37 −8.36 1.03 0.446]	12.6651	[4.0212 -53.4417]	1.0×10^{-2}	1.0×10^{0}	[0.905 −0.753 0.559 2.33]
ISS2	1.0×10^{-1}	1.0×10^{0}	[5.37 −8.36 1.03 0.446]	20.4289	[3.9795 -68.5728]	1.0×10^{-2}	1.0×10^{0}	[0.905 −0.753 0.559 2.33]
ISS3	1.0×10^{-1}	1.0×10^{0}	[5.37 −8.36 1.03 0.446]	4.7364	[4.1685 -14.3015]	1.0×10^{-2}	1.0×10^{0}	[0.905 −0.753 0.559 2.33]
ISS4	1.0×10^{-1}	1.0×10^{0}	[5.37 −8.36 1.03 0.446]	20.4289	[3.9795 -68.5728]	1.0×10^{-2}	1.0×10^{0}	[0.905 −0.753 0.559 2.33]
ISS5	1.0×10^{-1}	1.0×10^{0}	[5.37 −8.36 1.03 0.446]	22.1688	[3.9726 -70.7832]	1.0×10^{-2}	1.0×10^{0}	[0.905 −0.753 0.559 2.33]
ISS6	1.0×10^{-1}	1.0×10^{0}	[5.37 −8.36 1.03 0.446]	4.7364	[4.1685 -14.3015]	1.0×10^{-2}	1.0×10^{0}	[0.905 −0.753 0.559 2.33]

Table 5
Energy generated [J] in each sea state (ISS1–ISS6) for the H_2, passive, reactive, and H_∞ controllers. The H_2 strategy achieves the highest overall energy production across all conditions.

Sea State	H_2	Passive	Reactive	H_∞
ISS1	14.5121	7.9051	14.3200	2.6842
ISS2	46.9913	17.9869	47.5906	4.3308
ISS3	1.2019	1.0127	1.0598	0.6517
ISS4	0.8570	0.3665	0.8195	0.1239
ISS5	4.6036	1.8538	4.3948	0.6225
ISS6	0.1483	0.1277	0.1285	0.0895
Total Energy	**68.3142**	**29.2527**	**68.3132**	**8.5026**

4.3. Controller performance assessment

In this study, we restricted the tuning process exclusively to the parameters β and ζ_2/ζ_∞. These parameters were selected through a logarithmic search within the intervals $[10^{-5}, 10^{0}]$ for β and $[10^{0}, 10^{10}]$ for both ζ_2 and ζ_∞. These ranges were defined based on empirical observations of values for which the corresponding LMI problems typically yield feasible solutions. The optimisation of the LMI conditions was performed using a self-dual embedding interior-point method based on self-concordance, which efficiently solves convex conic problems. For each robust controller, H_2 and H_∞, the decision variables β and ζ_2/ζ_∞ were tuned according to the power absorbed by the PTO, such that the selected parameters corresponded to those achieving the maximum energy extraction. Table 4 summarises the tuning parameters of all controllers.

Fig. 8 compares the performance of the controllers in terms of the WEC angular velocity and the corresponding control force. It can be observed that none of the controllers exceed the PTO operational limits in terms of maximum force or velocity. The H_∞ controller generally exacerbates the system motion across the considered sea states, with the exception of ISS2, for which the reactive and H_2 controllers achieve the best performance. Furthermore, an additional check is required to ensure physical feasibility with respect to the maximum PTO stroke. Fig. 9 indicates that none of the controllers extrapolates the PTO displacement limits for any of the considered sea states.

Fig. 10 illustrates the instantaneous power for sea states ISS1–ISS6, obtained under different control strategies, while Table 5 summarises the corresponding energy production for all cases. The reactive, H_2 and H_∞ controllers exhibit a characteristic behaviour in which power is occasionally injected back into the system during part of the cycle. This effect arises from the absence of explicit power constraints in the control design. In this regard, the H_∞ controller, when using the tuning parameters reported in Table 4, yields negative energy for some of the considered sea states. For this reason, the following additional constraints were imposed on the H_∞ controller: $G = G^\top \in \mathbb{R}^{n\times n}$, $G \geq \mathbf{I} \in \mathbb{R}^{n\times n}$, and $0 \leq Z_{ij} \leq 3$.

Although the H_∞ controller generally provides greater motion amplitudes, its tendency to inject power back into the system significantly compromises overall energy production. In contrast, the H_2 controller demonstrates a more well-behaved response, avoiding excessive motion amplification and maintaining positive power flow for most of the operating cycle. As a result, it naturally remains within the physical limits of the PTO while sustaining effective energy extraction.

The energy results reveal that the H_2 controller outperforms both the H_∞ and passive controllers in all cases, whereas the reactive controller achieves slightly higher energy production in ISS2. As shown in Table 4, identical robust control gains were applied across all sea states. This choice represents a realistic scenario, since, unless adaptive control techniques are employed, the same tuning would typically be implemented under varying sea conditions. Accordingly, a direct comparison with traditional WEC controllers should be interpreted in light of the fact that the passive and reactive controllers were tuned using the optimal IM-based gains interpolated at the peak frequency of each sea state, which tends to provide a favourable setting for these IM-based benchmarks.

Even under these favourable conditions for the passive controller, the proposed robust H_2 strategy achieved the highest total energy production when all sea states were considered. As reported in Table 5, the H_2 controller yielded approximately 0.0015%, 133.5%, and 703.5% higher total energy production compared with the reactive, passive and H_∞ benchmark controllers, respectively.

5. Conclusion

The results presented in this work demonstrate the effectiveness of the proposed robust H_2 controller for wave energy conversion. The controller exhibited satisfactory performance compared with the classical WEC passive/reactive control strategies and the traditional robust H_∞ controller. Additionally, the H_2 approach achieved higher overall energy capture while maintaining an acceptable control effort and adhering to the physical limits of the system. The hypothesis that the H_2 for-

mulation would perform well in wave energy systems, due to its inherent ability to consider the average contribution of all excitation frequencies; was confirmed through the results obtained. Unlike the H_∞ controller, which focuses on worst-case scenarios, the H_2 approach ensures an optimal balance between energy absorption and robustness under stochastic sea-state conditions. Additionally, we have shown that it is possible to achieve these results by tuning only two parameters, β and ζ_2, in a manner conceptually similar to the tuning of conventional PID controllers. This simplicity highlights the practicality and ease of implementation of the proposed control approach.

Furthermore, the limitations associated with causal implementations of the impedance-matching principle, modelling uncertainties, and the general approximations required in model-based control frameworks support the argument for adopting data-driven strategies in wave energy applications. This study serves as an illustration of such an approach, demonstrating that effective control design can be achieved directly from experimental data while maintaining physical feasibility and interpretability. Nevertheless, this study has also highlighted that even data-driven approaches are subject to uncertainties, ultimately reinforcing the need to incorporate robustness into WEC controller design.

Future work will focus on extending the proposed framework to incorporate explicit constraints on the system states and control inputs, ensuring compliance with the physical limits of the WEC and PTO. Additionally, further investigations will compare the proposed approach with other advanced control techniques recently explored in the WEC literature, such as optimal spectral-based and Symphony control strategies.

CRediT authorship contribution statement

Josefredo Gadelha Da Silva: Writing – original draft, Visualization, Validation, Software, Methodology, Investigation, Formal analysis, Conceptualization; **Marcio Junior Lacerda:** Writing – review & editing, Supervision, Software, Methodology, Formal analysis, Conceptualization; **Matheus Costa:** Visualization, Validation, Methodology; **Erivelton Nepomuceno:** Writing – review & editing, Supervision, Project administration, Methodology, Investigation, Funding acquisition.

Declaration of competing interest

The authors declare that they have no known competing financial interests or personal relationships that could have appeared to influence the work reported in this paper.

Josefredo Gadelha da Silva, Matheus Costa and Erivelton Nepomuceno report that support was provided by Taighde Éireann - Research Ireland. Erivelton Nepomuceno also reports that support was provided by the Conselho Nacional de Desenvolvimento Científico e Tecnológico. These funds were awarded by national research agencies to support impartial scientific work and are not considered competing interests. If there are other authors, they declare that they have no known competing financial interests or personal relationships that could have appeared to influence the work reported in this paper.

Acknowledgment

This work was supported by Taighde Éireann - Research Ireland (Grant 21/FFP-P/10065). For Open Access, the author has applied a CC BY public copyright licence to any Author Accepted Manuscript arising from this submission. E. Nepomuceno was also supported by CNPq, Brazil (Grant 444154/2024-8). Josefredo Silva acknowledges the postdoctoral researchers at the Centre for Ocean Energy Research for their willingness to clarify, on some occasions, questions concerning fundamental aspects of WEC control. Special thanks are extended to Pedro Fornaro for his assistance in this regard.

References

Agulhari, C.M., Felipe, A., Oliveira, R.C.L.F., Peres, P.L.D., 2019. Algorithm 998: The Robust LMI Parser – A toolbox to construct LMI conditions for uncertain systems. ACM Transactions on Mathematical Software 45 (3), 36:1-36:25. https://doi.org/10.1145/3323925

Agulhari, C.M., Oliveira, R. C.L.F., Peres, P. L.D., 2010. Static output feedback control of polytopic systems using polynomial Lyapunov functions. In: 49th IEEE Conference on Decision and Control (CDC), pp. 6894–6901. https://doi.org/10.1109/CDC.2010.5717214

Anderlini, E., Forehand, D.I.M., Bannon, E., Abusara, M., 2017. Reactive control of a wave energy converter using artificial neural networks. Int. J. Mar. Energy 19, 207–220. https://doi.org/10.1016/j.ijome.2017.08.001

Celesti, M.L., Ferri, F., Faedo, N., 2024. Experimental modelling uncertainty quantification for a prototype wave energy converter. In: 2024 European Control Conference (ECC), pp. 1546–1551. https://doi.org/10.23919/ECC64448.2024.10590984

Davidson, J., Costello, R., 2020. Efficient nonlinear hydrodynamic models for wave energy converter design–a scoping study. J. Mar. Sci. Eng. 8 (1). https://doi.org/10.3390/jmse8010035

deOliveira, M.C., Skelton, R.E., 2001. Stability tests for constrained linear systems. In: Reza Moheimani, S.O. (Ed.), Perspectives in Robust Control. Springer-Verlag, New York, NY. Vol. 268 of *Lecture Notes in Control and Information Science*, pp. 241–257.

Faedo, N., Carapellese, F., Pasta, E., Mattiazzo, G., 2022. On the principle of impedance-matching for underactuated wave energy harvesting systems. Appl. Ocean Res. 118, 102958. https://doi.org/10.1016/j.apor.2021.102958

Faedo, N., Celesti, M.L., 2024. On the role of modelling uncertainty in optimal control and performance assessment of wave energy conversion systems. In: ISOPE International Ocean and Polar Engineering Conference. ISOPE, pp. ISOPE–I.

Faedo, N., García-Violini, D., Scarciotti, G., Astolfi, A., Ringwood, J.V., 2019. Robust moment-based energy-maximising optimal control of wave energy converters. In: 2019 IEEE 58th Conference on Decision and Control (CDC), pp. 4286–4291. https://doi.org/10.1109/CDC40024.2019.9029578

Faedo, N., Peña-Sanchez, Y., Carapellese, F., Mattiazzo, G., Ringwood, J.V., 2021. LMI-based passivation of lti systems with application to marine structures. IET Renewable Power Gener. 15 (14), 3424–3433. https://doi.org/10.1049/rpg2.12286

Faedo, N., Peña-Sanchez, Y., Garcia-Violini, D., Ferri, F., Mattiazzo, G., Ringwood, J.V., 2023a. Experimental assessment and validation of energy-maximising moment-based optimal control for a prototype wave energy converter. Control Eng. Pract. 133, 105454. https://doi.org/10.1016/j.conengprac.2023.105454

Faedo, N., Peña-Sanchez, Y., Pasta, E., Papini, G., Mosquera, F.D., Ferri, F., 2023b. Swell: an open-access experimental dataset for arrays of wave energy conversion systems. Renewable Energy 212, 699–716. https://doi.org/10.1016/j.renene.2023.05.069

Falnes, J., 2002. Ocean Waves and Oscillating Systems: Linear Interactions Including Wave-Energy Extraction. Cambridge University Press. https://doi.org/10.1017/CBO9780511754630

Farajvand, M., Grazioso, V., García-Violini, D., Ringwood, J.V., 2023. Uncertainty estimation in wave energy systems with applications in robust energy maximising control. Renewable Energy 203, 194–204. https://doi.org/10.1016/j.renene.2022.12.054

Fusco, F., Ringwood, J.V., 2013. A simple and effective real-time controller for wave energy converters. IEEE Trans. Sustainable Energy 4 (1), 21–30. https://doi.org/10.1109/TSTE.2012.2196717

Garcia-Violini, D., Ringwood, J.V., 2021. Energy maximising robust control for spectral and pseudospectral methods with application to wave energy systems. Int. J. Control 94 (4), 1102–1113. https://doi.org/10.1080/00207179.2019.1632491

García-Violini, D., Peña-Sanchez, Y., Faedo, N., Ringwood, J.V., 2020a. An energy-maximising linear time invariant controller (lite-con) for wave energy devices. IEEE Trans. Sustainable Energy 11 (4), 2713–2721. https://doi.org/10.1109/TSTE.2020.2971392

García-Violini, D., Peña-Sanchez, Y., Faedo, N., Windt, C., Ferri, F., Ringwood, J.V., 2021. Experimental implementation and validation of a broadband LTI energy-maximizing control strategy for the wavestar device. IEEE Trans. Control Syst. Technol. 29 (6), 2609–2621. https://doi.org/10.1109/TCST.2021.3052479

García-Violini, D., Peña-Sanchez, Y., Faedo, N., Windt, C., Ringwood, J.V., 2020b. LTI energy-maximising control for the wave star wave energy converter: identification, design, and implementation. IFAC-PapersOnLine 53 (2), 12313–12318. 21st IFAC World Congress. https://doi.org/10.1016/j.ifacol.2020.12.1193

Gustavsen, B., Semlyen, A., 1999. Rational approximation of frequency domain responses by vector fitting. IEEE Trans. Power Delivery 14 (3), 1052–1061.

Lao, Y., Scruggs, J.T., 2020. Robust control of wave energy converters using unstructured uncertainty. In: 2020 American Control Conference (ACC), pp. 4237–4244. https://doi.org/10.23919/ACC45564.2020.9148045

Levy, E.C., 1959. Complex-curve fitting. IRE Trans. Autom. Control 4 (1), 37–43.

Li, H., Ding, H., Chang, T., Chen, L., 2025. H2-norm optimization and performance assessment of a jacket offshore platform under coupled wind-wave-seismic excitations via track mono-, bi- and tri-stable nonlinear energy sink cells. Ocean Eng. 336, 121671. https://doi.org/10.1016/j.oceaneng.2025.121671

Liu, S., Papanikolaou, A.D., 2011. Time-domain hybrid method for simulating large amplitude motions of ships advancing in waves. Int. J. Nav. Archit. Ocean Eng. 3 (1), 72–79. https://doi.org/10.2478/JNAOE-2013-0047

Ljung, L., 1999. System Identification: Theory for the User. Prentice Hall PTR, Upper Saddle River, NJ. 2nd edition.

Löfberg, J., 2004. Yalmip : a toolbox for modeling and optimization in matlab. In: In Proceedings of the CACSD Conference. Taipei, Taiwan. https://doi.org/10.1109/CACSD.2004.1393890

Martin, D., Tai, W., Zuo, L., 2018. Stabilized Offshore Floating Wind Platform Using a Dual-Function Wave Energy Converter. In: 4th Asian Wave and Tidal Energy Conference (AWTEC). Taipei, Taiwan. AWTEC.

McKelvey, T., Akçay, H., Ljung, L., 1996. Subspace-based identification from frequency response data. IEEE Trans. Autom. Control 41 (7), 960–979.

Ning, D., Ding, B., 2022. Modelling and Optimization of Wave Energy Converters. CRC Press.

Papillon, L., Costello, R., Ringwood, J.V., 2020. Boundary element and integral methods in potential flow theory: a review with a focus on wave energy applications. J. Ocean Eng. Mar. Energy 6, 303–337. https://doi.org/10.1007/s40722-020-00175-7

Pintelon, R., Schoukens, J., 2012. System Identification: A Frequency Domain Approach. Wiley-IEEE Press, Hoboken, NJ. 2nd edition.

Ringwood, J.V., Merigaud, A., Faedo, N., Fusco, F., 2018. Wave energy control systems: Robustness issues. IFAC-PapersOnLine 51 (29), 62–67. 11th IFAC Conference on Control Applications in Marine Systems, Robotics, and Vehicles CAMS 2018. https://doi.org/10.1016/j.ifacol.2018.09.470

Ringwood, J.V., Zhan, S., Faedo, N., 2023. Empowering wave energy with control technology: Possibilities and pitfalls. Annu. Rev. Control 55, 18–44. https://doi.org/10.1016/j.arcontrol.2023.04.004

da Silva, J.G., Lacerda, M.J., Bertolin, A. L.J., Nazaré, T., Costa, M., Nepomuceno, E., 2025. H∞ control co-design for uncertain polytopic systems. ASME Lett. Dyn. Syst. Control 5 (3), 030905. https://doi.org/10.1115/1.4068615

Sturm, J.F., 1999. Using sedumi 1.02, a MATLAB toolbox for optimization over symmetric cones. Optim. Methods Software 11 (1-4), 625–653. https://doi.org/10.1080/10556789908805766

Sun, T., Liao, Z., Al-Ani, M., Jordan, L.-B., Li, G., Zhan, S., Belmont, M., Edwards, C., 2023. Modelling and control tank testing validation for attenuator type wave energy converter - part III: Model predictive control and robustness validation. IEEE Trans. Sustainable Energy 14 (3), 1737–1746. https://doi.org/10.1109/TSTE.2023.3246171

Welch, P.D., 1967. The use of fast fourier transform for the estimation of power spectra: A method based on time averaging over short, modified periodograms. IEEE Trans. Audio Electroacoust. 15 (2), 70–73. https://doi.org/10.1109/TAU.1967.1161901

Windt, C., Faedo, N., Penalba, M., Dias, F., Ringwood, J.V., 2021. Reactive control of wave energy devices - the modelling paradox. Appl. Ocean Res. 109, 102574. https://doi.org/10.1016/j.apor.2021.102574

Wolgamot, H.A., Fitzgerald, C.J., 2015. Nonlinear hydrodynamic and real fluid effects on wave energy converters. Proc. Inst. Mech. Eng. Part A: J. Power Energy 229 (7), 772–794.

Zhou, K., Doyle, J.C., 1998. Essentials of Robust Control. Vol. 104. Prentice hall Upper Saddle River, NJ.

Zou, S., Zhou, X., Weaver, W., Abdelkhalik, O., 2022. Deep reinforcement learning control of wave energy converters. IFAC-PapersOnLine 55 (27), 305–310. 9th IFAC Symposium on Mechatronic Systems MECHATRONICS 2022. https://doi.org/10.1016/j.ifacol.2022.10.530